J. Ocean Univ. China (Oceanic and Coastal Sea Research)
https://doi.org/10.1007/s11802-024-5566-4
ISSN 1672-5182, 2024 23 (3): 661-675
http://www.ouc.edu.cn/xbywb/
E-mail:xbywb@ouc.edu.cn

Numerical Simulation on Production Trials by Using Depressurization for Typical Marine Hydrate Reservoirs: Well Type and Formation Dip

QIN Fanfan[1)], SUN Jiaxin[1), *], GU Yuhang[1)], CAO Xinxin[1)], MAO Peixiao[1)], NING Fulong[1), 2)], and JIANG Guosheng[1)]

1) *National Center for International Research on Deep Earth Drilling and Resource Development*, *Faculty of Engineering*, *China University of Geosciences*, *Wuhan* 430074, *China*
2) *Laboratory for Marine Mineral Resources*, *Qingdao National Laboratory for Marine Science and Technology*, *Qingdao* 266237, *China*

(Received October 14, 2022; revised January 20, 2023; accepted February 19, 2023)

Abstract Natural gas hydrate has huge reserves and is widely distributed in marine environment. Its commercial development is of great significance for alleviating the contradiction between energy supply and demand. As an efficient research method, numerical simulation can provide valuable insights for the design and optimization of hydrate development. However, most of the current production models simplify the reservoir as a two-dimensional (2D) horizontal layered model, often ignoring the impact of formation dip angle. To improve the accuracy of production prediction and provide theoretical support for the optimization of production well design, two three-dimensional (3D) geological models with different dip angles based on the geological data from two typical sites are constructed. The vertical well, horizontal well and multilateral wells are deployed in these reservoirs with different permeabilities to perform production trial, and the sensitivity analysis of dip angles is also carried out. The short-term production behaviors in high and low permeability reservoirs with different dip angles are exhibited. The simulation results show that 1) the gas and water production behaviors for different well types in the two typical reservoirs show obviously different variation laws when the short-term depressurization is conducted in the inclined formation; 2) the inclined formation will reduce the gas production and increase the water extraction, and the phenomena becomes pronounced as the dip angle increases, particularly in the low-permeability reservoirs; 3) and the impact of formation dip on hydrate recovery does not change significantly with the variation of well type.

Key words natural gas hydrate; inclined formation; depressurization; production well type

1 Introduction

Natural gas hydrate (hereinafter referred to as hydrate) is an ice-like cage compound formed by natural gas molecules and water molecules under low temperature and high-pressure conditions (Sloan, 2003). It has the advantages of wide distribution, huge reserves, clean and pollution-free combustion, and mainly occurs in the marine and permafrost areas (Song *et al.*, 2014). In general, a unit volume of hydrate can release about 160 volumes of methane gas, so it is considered as one of the most potential alternative energy sources to alleviate the global energy crisis (Sun *et al.*, 2021b; Xu *et al.*, 2021). In addition, hydrate has been listed as the 173rd mineral by China in November 2017, which further accelerates the industrialization process of hydrate in China (Ning *et al.*, 2020).

At present, several countries around the world have carried out hydrate production trials in various regions (Li *et al.*, 2016), such as the Mackenzie Delta in Canada (Hancock *et al.*, 2005; Yamamoto and Dallimore, 2008), the north slope of Alaska in the USA (Schoderbek *et al.*, 2013), Nankai Trough in Japan (Boswell, 2013; Yamamoto *et al.*, 2019), and the South China Sea and Qilian Mountain permafrost regions in China (Li *et al.*, 2018; Wang *et al.*, 2018). However, the gas recovery of these production trials is relatively low, and it is difficult to meet the standards of commercial production. Therefore, the stimulation of gas production has become one of the hot issues in current researches (Wu *et al.*, 2018; Li *et al.*, 2019a, b; Chen *et al.*, 2020b; Sun *et al.*, 2021c; Huang *et al.*, 2022; Ji *et al.*, 2022).

Numerical simulation, as an effective method to study natural gas hydrates, has the advantages of low cost and short time span. It can quickly reveal the formation and dissociation mechanisms of hydrates (Sun *et al.*, 2015; Li *et al.*, 2018b; Mi *et al.*, 2022a, b, c; Zhang *et al.*, 2022), analyze the geomechanical response of the reservoir during the production process (Sun *et al.*, 2017, 2018; Dong *et al.*, 2019; Dou *et al.*, 2020), predict the production potential

* Corresponding author. E-mail: jiaxinsun@cug.edu.cn

under different stimulation methods and carry out the sensitivity analysis of various factors (Sun *et al.*, 2019, 2022; Ning *et al.*, 2022). However, in order to facilitate the model construction, the actual geological body is usually simplified. For example, in productivity prediction, the hydrate reservoir is typically simplified into a 2D horizontal formation model or a cylindrical model. Nevertheless, this simplification may ignore the possible influence of some physical and chemical properties of the actual formation on the hydrate production behavior.

In previous simulation studies, the influence of reservoir physical properties and production methods on gas recovery has been investigated in detail (Bu *et al.*, 2021; Sun *et al.*, 2021a; Cao *et al.*, 2022; Gu *et al.*, 2022, 2023). However, the formation dip, a key factor in modeling, is rarely considered. In fact, most hydrate reservoirs in marine environments have a certain degree of formation fluctuation, and only a few works have analyzed the impact of this factor on hydrate recovery. For example, Kurihara *et al.* (2010) constructed a 3D model of a hydrate reservoir by combining the logging data and seismic data of sediments in the eastern Nankai Trough of Japan, and the effects of fault, dip angle, reservoir permeability and well location on the production performance were studied. They found that large-scale distributed formation heterogeneity features, such as the presence of faults and formation fluctuations, will significantly affect short-term production behavior. Yuan *et al.* (2018) also established a prediction model for the exploitation of the inclined hydrate reservoir based on the survey data from the Shenhu area in the South China Sea. The simulation results showed that the gas production behavior of hydrate deposits is sensitive to pressure change, and the formation dip is one of the important factors affecting the recovery of gas and water. After that, Song *et al.* (2019) built a 3D multi-field coupling model considering the weakening of formation strength during hydrate dissociation based on the exploration data from the Shenhu area in the South China Sea, and found that the slope is more stable and the gas production is higher when the horizontal wells are oriented in the vertical slope direction. Then, Chen *et al.* (2020a) further studied the effects of formation dip and horizontal reservoir parameter heterogeneity on gas production, and found that when the dip is 10 degrees, the equivalent permeability of the reservoir should be reduced by 50% to achieve the same production rate. Based on a 2D hydrate inclined formation model, Mao *et al.* (2021a) recently compared the production performance of horizontal wells deployed in different structural positions and found that the productivity is higher when the wells are laid in the lower part of the reservoir structure.

According to the above investigations, the impact of formation dip on the production performance of hydrate reservoirs has not yet been fully clarified, and there is few systematic and comprehensive analysis of the response behavior under different well conditions in the formations with various dip angles. This paper takes the marine hydrate reservoir as the research object and examines two typical reservoirs with different permeabilities at site AT1 in the eastern Nankai Trough of Japan and site W11 in the South China Sea, which aims to explore the potential differences between them. Specifically, we construct the 3D inclined reservoir models and systematically study the impact of changes in the reservoir dip on the short-term production performance. In addition, the production behaviors of different well types in inclined formations are also discussed, which can provide some references for the subsequent model construction, improve the accuracy of production prediction, and better serve the optimization design of the actual production trials for different marine reservoirs.

2 Numerical Model

2.1 Geological Background

In this study, two typical hydrate reservoirs, site AT1 in the eastern Nankai Trough of Japan and site W11 in the South China Sea, are selected for short-term production using depressurization. As we know, the former is a typical sandy reservoir with high permeability, while the latter is a typical silty reservoir with low permeability. Both sites have a certain formation dip (Fig.1). According to the field survey data, the dip angles at both sites are about 10 degrees. The geological characteristics of two typical marine hydrate reservoirs are as follows:

1) Site AT1 in the eastern Nankai Trough of Japan (Fig.

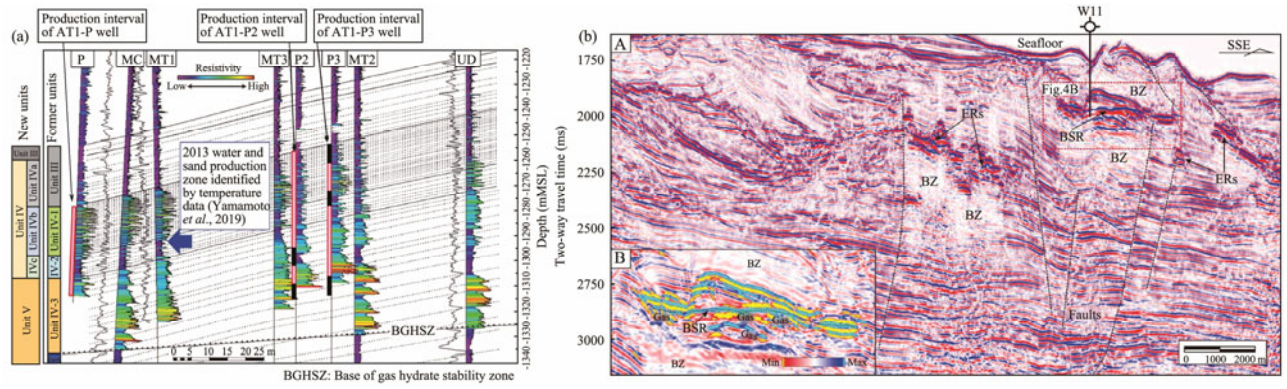

Fig.1 Exploration results of site AT1 (a) in the eastern Nankai Trough of Japan and site W11 (b) in the South China Sea (Yamamoto *et al*., 2019; Zhang *et al*., 2020).

1a): At this site, hydrate mainly occurs in sediments with high permeability, located in the north slope of Daini-Atsumi Knoll in eastern Nankai Trough, Japan. Also, the water depth is 998 m, and gas hydrate is found at 276–338 m below the seafloor (mbsf), mainly Type I hydrate, with a total thickness of about 62 m, a porosity of 0.30–0.42, and a maximum saturation of 90% (Sun *et al.*, 2016). The formation is mainly composed of loose sediments, with foliated and sheeted strata in the upper part and channel sand sequence in the lower part (Fujii *et al.*, 2013). The sea bottom temperature is about 2.8–3.0℃, and the geothermal gradient is 29.97–33.36℃ km^{-1}.

2) Site W11 in the South China Sea (Fig.1b): Here is a low-permeability hydrate reservoir located in the Shenhu area of the Pearl River Mouth Basin in the north of the South China Sea (Zhang *et al.*, 2020). Also, the water depth is 1309.75 m, and hydrate occurs at 116.5–192.5 mbsf, with a total thickness of about 76 m, a relatively low formation permeability of about 0.22 mD, a porosity of about 0.345, and an average hydrate saturation of 0.34. The formation is mainly composed of silty clay, in which the clay content is 14.2%–38.7% and the silt content is 61.1%–83.0% (Mao *et al.*, 2021b).

2.2 Model Construction

In this investigation, TOUGH+HYDRATE software is employed to simulate the production behaviors of the two reservoirs. By solving the mass and heat conservation equations, the software can invoke the equilibrium model or dynamic model of hydrate formation and dissociation to carry out specific studies, which is suitable for complex geological bodies conforming to Darcy's law (Moridis, 2008). Because of the large number of grid division in this study, the parallel version of the software is used for prediction. The equilibrium model is adopted in the simulation, and prediction and analysis are mainly made for the thermal-fluid-chemical multi-field coupling process of the hydrate reservoir. It is assumed that the borehole is stable and the sand control is reliable. As the simulation time is relatively short, the geomechanical response is not considered at present.

In the specific study, Model A is defined as a high-permeability hydrate reservoir based on the geological data from site AT1 in the eastern Nankai Trough of Japan (Fig. 2a). The model consists of a hydrate reservoir with a thickness of 62 m and a hydrate-free overburden/underburden with a thickness of 276 m. The survey data show that the hydrate reservoir can be roughly divided into three layers from top to bottom according to the formation lithology, labeled as GHBS1, GHBS2 and GHBS3, with the reservoir thickness of 14 m, 15 m, and 33 m respectively. For GHBS1, the porosity is 0.41, the permeability is $k_x=k_y=1100$ mD, $k_z=500$ mD, and the saturation is 0.6; for GHBS2, the porosity is 0.42, the permeability is $k_x=k_y=40$ mD, $k_z=20$ mD, and the saturation is 0.35; for GHBS3, the porosity is 0.42, the permeability is $k_x=k_y=1100$ mD, $k_z=800$ mD, and the saturation is 0.7. The thickness of the overburden/underburden is set by the reservoir buried depth, which ensures that the hydrate reservoir can accurately exchange heat and transfer pressure with the surrounding formations (Sun *et al.*, 2022). The total thickness of the model in the z-axis direction is 614 m, and the projection length of the hypotenuse along the horizontal direction is 200 m × 200 m. Due to the high computational cost of the complete model, half of the model is taken for study according to its symmetry in the y-axis direction. The borehole radius is set to 0.108 m, and the detailed parameters of the reservoir are shown in Table 1.

Meanwhile, Model B is defined as a low-permeability hydrate reservoir, which is built on the basis of the geological data from site W11 in the South China Sea (Fig.2b). Similarly, the model consists of a hydrate layer with a thickness of 76 m and a hydrate-free overburden/underburden with a thickness of 116.5 m. Due to the lack of more detailed geological data, the hydrate reservoir is treated as a homogeneous geological body in this study. The porosity of the hydrate layer is 0.345, the per meability is $k_x=k_y=k_z=0.22$ mD, and the saturation is 0.34. For the same reason reason, the thickness of the overburden/underburden is set by the reservoir buried depth. Therefore, the total thick-

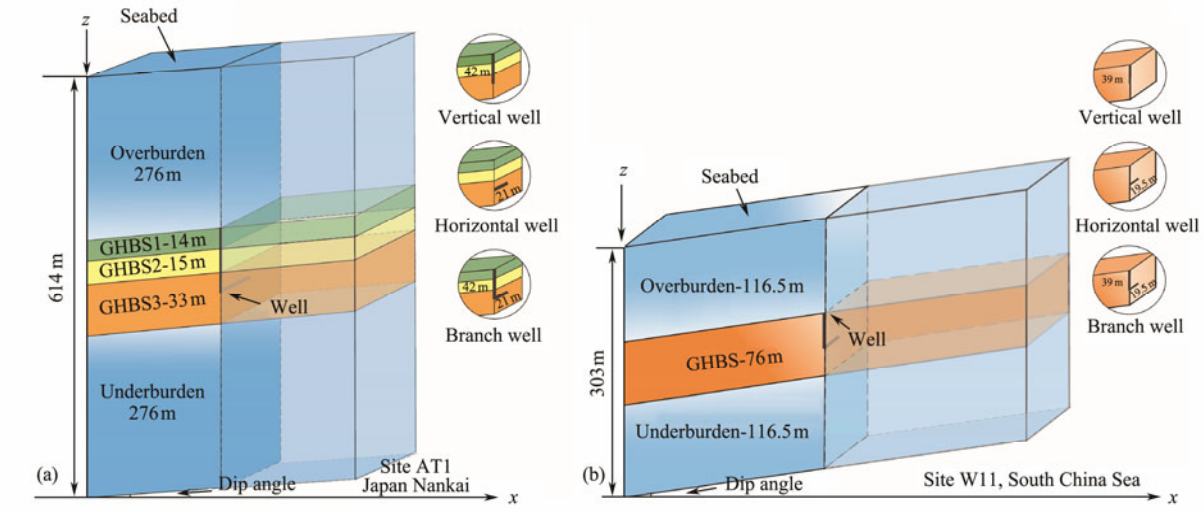

Fig.2 Schematic diagram of hydrate reservoir production model at site AT1 (a) and site W11 (b).

ness of the model in the *z*-axis direction is 309 m, and the projection length of the hypotenuse along the horizontal direction is 500 m × 500 m. Similarly, half of the model is taken for simulation according to its symmetry. The borehole radius is set to 0.1 m, and the specific parameters of the reservoir are shown in Table 2.

Table 1 Parameters used in the simulation model for site AT1 in eastern Nankai Trough of Japan (Sun *et al*., 2016)

Parameter	Value	Parameter	Value
Overburden thickness	276 m	Grain specific heat	792 J kg ℃$^{-1}$
Underburden thickness	276 m	Wet thermal conductivity (sand & silt)	2.917 W m^{-1} ℃$^{-1}$
GHBS1 thickness	14 m	Wet thermal conductivity (clay & mud)	1.7 W m^{-1} ℃$^{-1}$
GHBS2 thickness	15 m	Dry thermal conductivity	1.0 W m^{-1} ℃$^{-1}$
GHBS3 thickness	33 m	Intrinsic permeability of GHBS1	$k_x=k_y=1100$ mD $k_z=500$ mD
Borehole radius	0.108 m		
Bottomhole pressure	4.5 MPa	Intrinsic permeability of GHBS2	$k_x=k_y=40$ mD $k_z=20$ mD
Initial bottom temperature of GHBS3	13.72℃		
Initial bottom pressure of GHBS3	13.52 MPa	Intrinsic permeabilities of GHBS3 and underburden	$k_x=k_y=1000$ mD $k_z=800$ mD
Water salinity	3.50%		
Initial saturation in GHBS1	$S_{H1}=0.60$ $S_{A1}=0.40$	Intrinsic permeability of overburden	$k_x=k_y=k_y=10$ mD
		Composite thermal conductivity model	$\lambda c=\lambda_{Hs}+(S_A^{1/2}+S_H^{1/2})(\lambda_s-\lambda_{Hs})+\Phi S_I\lambda_I$
Initial saturation in GHBS2	$S_{H2}=0.35$ $S_{A2}=0.65$	Capillary pressure model	$P_{cap}=-P_0[(S^*)]^{-1/\lambda}]-1]^{1-\lambda}$ $S^*=(S_A-S_{irA})/(S_{mxA}-S_{irA})$
		S_{mxA}	1
Initial saturation in GHBS3	$S_{H3}=0.70$ $S_{A3}=0.30$	λ	0.45 (sand), 0.15 (clay/mud)
		P_0	10^4 Pa (sand), 10^5 Pa (clay/mud)
Porosity of overburden	0.43	Relative permeability model	$k_{rA}=[(S_A-S_{irA})/(1-S_{irA})]^n$ $k_{rG}=[(S_G-S_{irG})/(1-S_{irA})]^{nG}$
Porosity of GHBS1	0.41		
Porosity of GHBS2	0.42	n	3.5 (sand), 5.0 (clay/mud)
Porosities of GHBS3 and underbuden	0.4		
Compression coefficient	1.00×10^{-8} Pa^{-1}	n_G	2.5 (sand), 3.0 (clay/mud)
Grain density	2650 kg m^{-3}	S_{irG}	0.01 (sand), 0.05 (clay/mud)
Geothermal gradient	30.0 K km^{-1}	S_{irA}	0.25 (sand), 0.55 (clay/mud)

Table 2 Simulation parameters of model for site W11 in South China Sea (Mao *et al*., 2021b)

Parameter	Value	Parameter	Value
Overburden thickness	116.5 m	Grain density	2650 kg m^{-3}
Thickness of the hydrate-bearing layer	76 m	Geothermal gradient	5.46℃ (100 m)$^{-1}$
Underburden thickness	116.5 m	Wet thermal conductivity	2.917 W m^{-1} ℃$^{-1}$
Porosity of the formation	34.50%	Dry thermal conductivity	1.00 W m^{-1} ℃$^{-1}$
Intrinsic permeability of the formation	$k_x=k_y=k_z=0.22$ mD	Compression coefficient	1.00×10^{-8} Pa^{-1}
Hydrate saturation	34.00%	Grain specific heat	1000 J kg^{-1} ℃$^{-1}$
S_{irA}	0.50	Water salinity	3.05%
S_{irG}	0.05	P_0	1.00×10^5 Pa
n_G	3	λ	0.15
Bottomhole pressure	4.50 MPa	S_{mxA}	1.00
Relative permeability model	$K_{rA}=(S_A^*)^n$ $K_{rG}=(S_G^*)^n$ $S_A^*=(S_A-S_{irA})/(1-S_{irA})$ $S_G^*=(S_G-S_{irG})/(1-S_{irA})$	Capillary pressure model	$P_{cap}=-P_0[(S^*)]^{-1/\lambda}]-1]^{1-\lambda}$ $S^*=(S_A-S_{irA})/(S_{mxA}-S_{irA})$

In addition, due to the relatively short production period, the lateral boundaries of the two models above can be approximated as adiabatic non-seepage boundaries, and the temperature and pressure at the upper and lower boundaries remain unchanged. Both models use a single depressurization method, and the bottomhole pressure is set to be 4.5 MPa. The production trial lasts 90 d, and this simulation time is long enough to effectively exhibit the short-term production behaviors.

2.3 Domain Discretization

The two models above are divided in the Cartesian coordinate system, with the mesh segmented into hexahedral block elements. Specifically, the variational method is adopted for mesh generation (Sun *et al.*, 2022). That is to say, the grid, typical of 5 m, is refined around the well and the reservoir area. The maximum grid size in the hydrate layer along the *z*-axis direction is 1.5 m, and the division is refined at the interface between the hydrate layer and the overburden/underburden to ensure the prediction accuracy. As mentioned above, to minimize the computation costs, half of the model area is studied according to its symmetry in the *y*-axis direction. Therefore, the specific grid division of models for the two reservoirs is as follows:

1) Model A: The size of the study area is 200 m (*x*) × 100 m (*y*) × 614 m (*z*), divided into 61 (*x*) × 60 (*y*) × 137 (*z*) =

501420 elements, including 7320 inactive grids. The thickness of the grids at the upper and lower boundaries of the model is 0.01 m.

2) Model B: The size of the study area is 500 m (x)×250 m (y)×309 m (z), divided into 63 (x)×60 (y)×97 (z)=366660 elements, including 7560 inactive grids. Also, the grids at the upper and lower boundaries of the model are 0.01 m in thickness.

2.4 Model Initialization

The proper initial conditions of the model are very important for the accuracy of the prediction results. In order to carry out comparative analysis, in this paper, we separately initialize the horizontal and inclined formation models. When initializing the pressure, it is assumed that the pore water in the reservoir is connected with the sea water, that is, the initial pore water pressure meets the hydrostatic pressure distribution. According to Eq. (1), the initial pressure distribution of the whole formation can be obtained.

$$P_{pw} = P_{atm} + \rho_{sw} g\left(h+z\right)\times 10^{-6}, \tag{1}$$

where P_{pw} represents the hydrostatic pressure, MPa; P_{atm} represents the standard atmospheric pressure, MPa; h represents the water depth, m; z is the formation depth below the seafloor, m; g is the acceleration of gravity, taken as 9.8 m s^{-2}; and ρ_{sw} is the average seawater density, taken as 1023 kg m^{-3}.

When performing the temperature initialization, the seafloor temperature is assumed to be constant (Mao *et al.*, 2021a). The specific temperature distribution of the whole model can be calculated according to Eq. (2) with the known seafloor temperature and the geothermal gradient. The temperature distribution of the inclined formation obtained by this method will present a certain angle with the horizontal formation, and the angle value is the formation dip.

$$T = T_0 + \Delta T \times z \times 10^{-3}, \tag{2}$$

where T_0 is the seabed temperature, ℃; and ΔT is the geothermal gradient, ℃ km^{-1}.

In addition, after the pressure and temperature distributions of the whole reservoir are calculated by the methods above, they need to be checked by the phase equilibrium (P-T) curve of methane hydrate to ensure that the pressure and temperature can keep the hydrate stable. According to the symmetry of the inclined formation model, only one inclined direction is considered for model construction. For example, the temperature and pressure initialization results of horizontal and inclined formations at site W11 in the South China Sea are shown in Fig.3.

2.5 Borehole Deployment and Scheme Design

In this investigation, the production performance is compared and analyzed, with three well types of single vertical well, horizontal well and multilateral wells deployed for two hydrate formations. The bottoms of the three type wells are located at the same depth of the reservoir, as shown in Fig.2. For the convenience of comparison, the effective production length of both vertical and horizontal wells is set to be 42 m at site AT1 referring to the design of wells in the first offshore production test, and the scheme of multilateral wells is composed of a 42 m vertical well section and two 21 m radial horizontal branches, with a total length of 84 m. For the site W11 in the South China Sea, the perforated intervals of vertical and horizontal well are

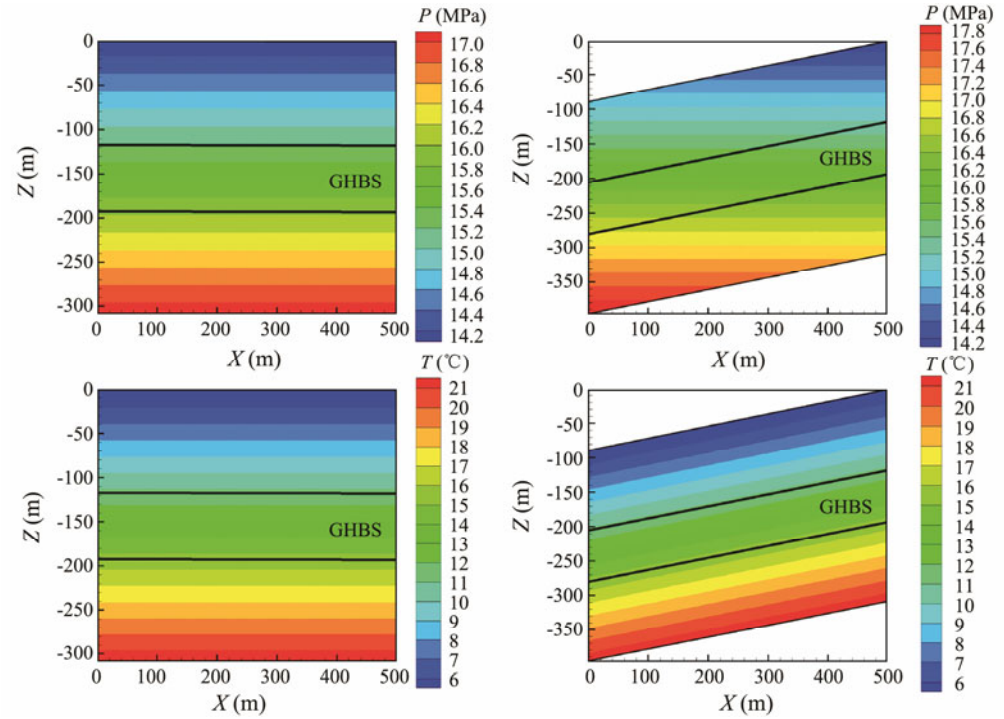

Fig.3 Initialization results of typical formation pressure and temperature.

both 39 m, and the deployment of multilateral wells is similar to that at site AT1, with a total length of 78 m.

As shown in Fig.4, the accuracy of the model parameters has been confirmed by matching the exploitation data within 6 days of the first offshore production trial at site AT1 (Sun *et al*., 2016). Therefore, based on the parameters above and some field measured data, this study will build typical production models for high and low permeability reservoirs, explore the influences of formation dip and production well type on the gas and water production in these two reservoirs, and make a comprehensive comparative analysis. As we know, site AT1 in eastern Nankai Trough is a typical sandy reservoir with high permeability, while site W11 in the South China Sea is a typical silty reservoir

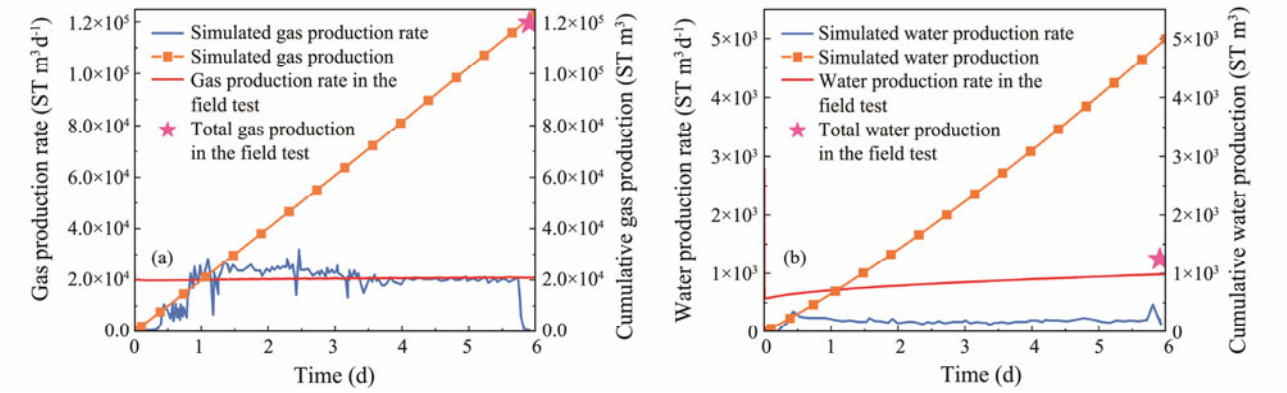

Fig.4 Comparative verification of test production results at site AT1 in the eastern Nankai Trough of Japan.

with low permeability. The investigations of these two representative marine sediments can give the universal research results. Specifically, according to the survey data (Yuan *et al*., 2018; Yamamoto *et al*., 2019; Zhang *et al*., 2020; Mao *et al*., 2021a), the formation dip angle in two reservoirs is about 10 degrees, and the maximum dip angle of the hydrate formation in the South China Sea does not exceed 25 degrees. Therefore, the formation dip values in the study are set as 0, 10, 20 and 30 degrees, and the well types include vertical well, horizontal well and radial multilateral wells, which are shown in Fig.2.

3 Results and Analyses

3.1 High-Permeability Hydrate Reservoir

3.1.1 Comparison for different types of wells

The types of production wells may have a significant impact on the production potential due to the variations in pressure drops in the reservoir. As mentioned above, the formation dip at site AT1 is about 10 degrees. Therefore, we focus on the comparison of the short-term production performances for three types of wells in this high-permeability inclined reservoir. As shown in Fig.5a, the gas production rates (Q_g) of vertical well and multilateral wells have relatively consistent evolution trends of gradual increase within 90 days. The average Q_g of multilateral wells and vertical well are 2.35×10^4 m^3 d^{-1} and 2.10×10^4 m^3 d^{-1}, respectively, and the Q_g of multilateral wells is 12.07% higher than that of vertical well. However, the Q_g of the horizontal well shows a trend of initially rising and then falling. It reaches its peak on the 67th day, close to 30000 m^3 d^{-1}, significantly higher than those of the vertical well and multilateral wells. Subsequently, it decreases rapidly to be lower than those of the vertical well and the multilateral wells and drops to about 15000 m^3 d^{-1} on the 90th day, with the average Q_g of about 19549 m^3 d^{-1} during the short-term production trial. Finally, the cumulative gas production (V_g) of the vertical well, horizontal well and multilateral wells is 1.89×10^6 m^3, 1.76×10^6 m^3 and 2.12×10^6 m^3, respectively, and the multilateral wells exhibit the highest gas production. Compared with the vertical well and horizontal well, gas production increases by about 12.07% and 20.34%, respectively. As for water production, the evolution trend of the water extraction rate (Q_w) of vertical well is very similar to that of multilateral wells, only with lower values of Q_w. In contrast, the Q_w of horizontal well keeps at the low values in the early stage, and increases significantly on the 65th day. The final water production (V_w) is about 2.02×10^5 m^3, 63.74% and 46.75% higher than that of the vertical well and the multilateral wells, respectively, as shown in Fig.5b. Fig.5c shows the evolution of the gas-to-water ratio (R_{gw}) over 90 days. It is obvious that the R_{gw} under the production scheme of multilateral wells is slightly greater than that under the vertical well production scheme. However, with the extension of the production cycle, they gradually tend to be consistent, while the R_{gw} using the horizontal well design is maximum in the first 75 days. After that, it rapidly falls below those of the vertical well and multilateral wells.

The phenomena described above can be explained by the spatial distributions of temperature and hydrate saturation in the reservoirs (Fig.6). Obviously, when the horizontal well is employed, the high permeability of the lowest hydrate layer will help to accelerate the convective heat transfer after depressurization. In addition, the pressure drop at the bottom hole rapidly transfers, which makes the Q_g increase rapidly. However, when the hydrate at the bottom of GHBS3 completely dissociates, the formation water in the underburden will flow into the GHBS3, which significantly weakens the depressurization effect. Furthermore, the amount of hydrate around the wells affected by

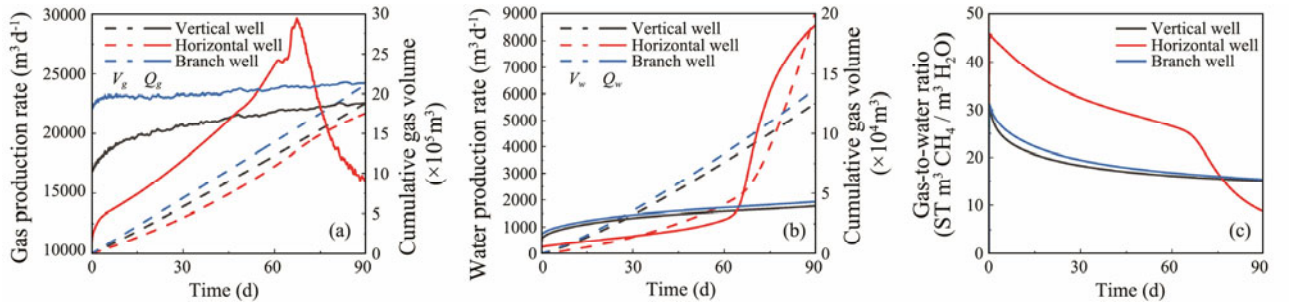

Fig.5 Gas and water production during short-term depressurization test at site AT1.

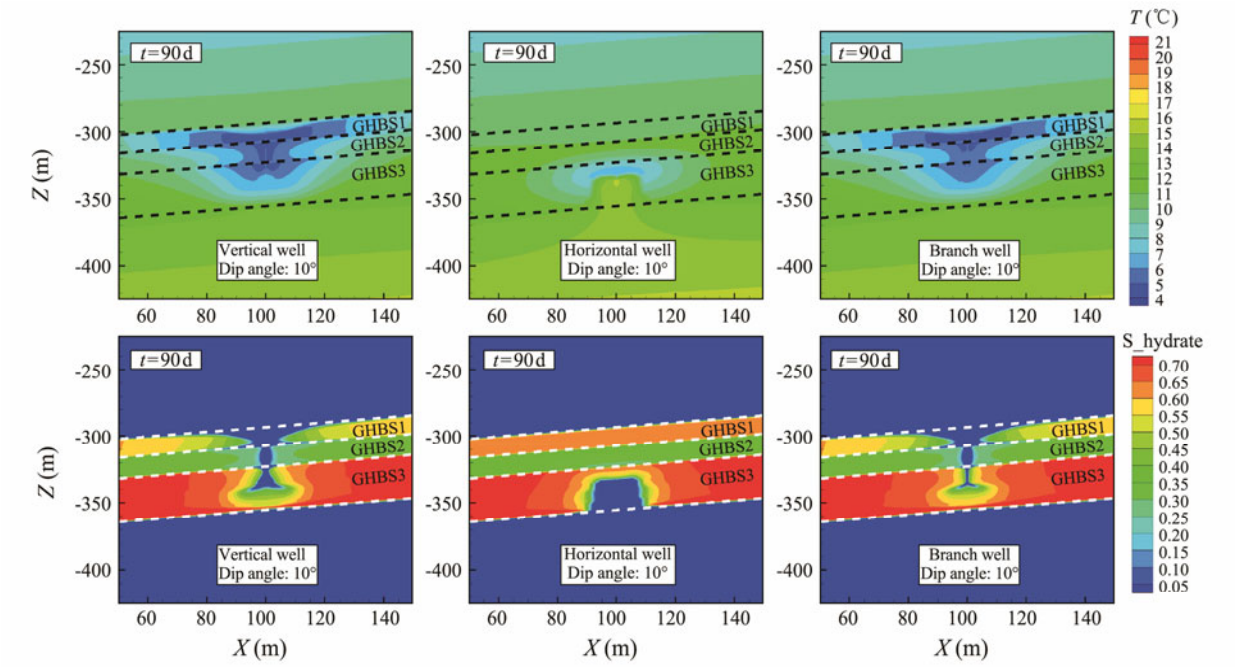

Fig.6 Spatial distributions of temperature and hydrate saturation under different well types at site AT1 (t=90 d, y=0 m).

thermal stimulation will gradually decrease, resulting in a continuous decline in the rate of hydrate dissociation, a reduction in the gas production, and a rapid increase in the water extraction. By contrast, the hydrate in the lower part of the reservoir does not completely dissociate when the vertical well and multilateral wells are used within 90 days, which forms a water-blocking area between the well and the underburden, resulting in the stable Q_g and Q_w. Additionally, because the perforated length of the multilateral wells is significantly extended, the corresponding Q_g and Q_w will increase. However, the multiples of increases for these two values are relatively similar, so the R_{gw} remains basically unchanged. When the horizontal well is adopted, the Q_w is relatively low in the early stage, which significantly improves the R_{gw}. As the gradual dissociation of hydrate in the lower part of the borehole, the invasion of water from the underlying formations leads to the decline in gas production and the increase in water extraction, resulting in a rapid decline in the corresponding R_{gw} below those of the vertical well and multilateral wells.

3.1.2 Influence of formation dip

In order to further clarify the influence of formation dip on the production behavior, Fig.7 shows the percentage increments of gas and water production for three well types in formations with different dips compared to horizontal sediment layers. Clearly, the law of gas production change is evidently consistent across the three types of production wells, and the cumulative gas production decreases with

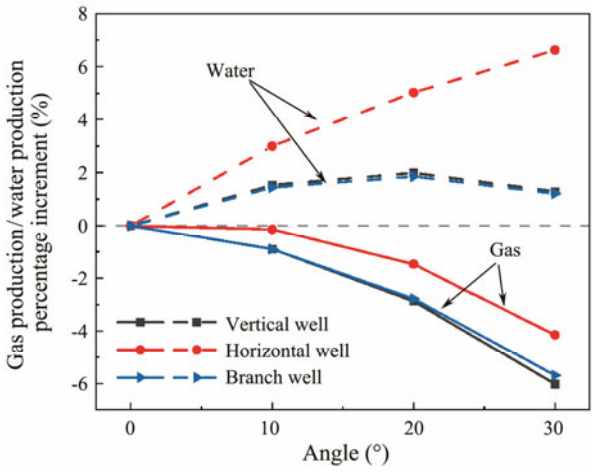

Fig.7 Percentage increments of gas and water production of inclined reservoir compared with horizontal formation at site AT1.

the increase of formation dip. To be specific, at the dip of 30 degrees, the production differences by the vertical well and multilateral wells both decrease by up to 6% compared with that from the horizontal formations. Moreover, the greater the dip, the more pronounced the decrease in gas production under the same dip difference. Besides, the reduction of gas recovery from the horizontal well is slightly lower than those from the vertical well and multilateral wells. The possible reason for these variations is that the pressure and gravity on both sides around the well will be different when the formation is tilted. The gas at the dissociation front on the relatively higher side can easily escape upward due to buoyancy, while the gas at the dissociation front on the relatively lower side must overcome the gravity of the surrounding water to achieve depressurization, resulting in a decrease in gas production (Figs.8 and 9). It is speculated that the low decline of gas production when the horizontal well is used in exploitation is attributed to the slight increase of hydrate dissociation in the inclined formation (Fig.8). Moreover, the increase of water production may also increase the dissolved gas extraction to a certain extent. Similarly, the cumulative water production from vertical well and multilateral wells shows almost the same increment, being the largest at the formation dip of 20 degrees, and the smallest in the horizontal formation. Most notably, the cumulative water production from the horizontal well increases near-linearly with the formation dip angle.

According to the predictions, during the short-term production trial of 90 days, the inclined reservoir will lead to a decrease in gas production, and the greater the formation dip, the more pronounced the decrease. The cumulative water production will increase with the formation dip angle. For the vertical well and multilateral wells, the cumulative water production will reach the highest when the dip angle is 20 degrees, which are about 2% higher than that of the horizontal formation. If the horizontal well is used, the largest increase will be achieved at 30 degrees, which is about 6.62% higher than that of the horizontal formation. Therefore, the boreholes are suggested to be deployed in the horizontal reservoir as far as possible.

3.2 Low-Permeability Hydrate Reservoir

3.2.1 Comparison for different types of wells

Fig.10 also shows the evolutions of gas production, water extraction and R_{gw} from three types of production wells within 90 days at site W11 in the South China Sea when the formation dip is 10 degrees. In this low-permeability reservoir, the variation trends of Q_g for the three production well types are basically the same, and all the Q_g are relatively low, as shown in Fig.10a. According to the predictions, the Q_g under the scheme of multilateral wells is the highest, and the corresponding V_g within 90 days is 8129.27 m^3. The V_g of the horizontal well is about 4717.88 m^3, which is about 41.96% lower than that of the multilateral wells. However, the gas production of the vertical well is the lowest, and the final V_g is only 3639.91 m^3, which is about 55.22% lower than that of the multilateral wells. The possible reason for these results is that the perforated in-

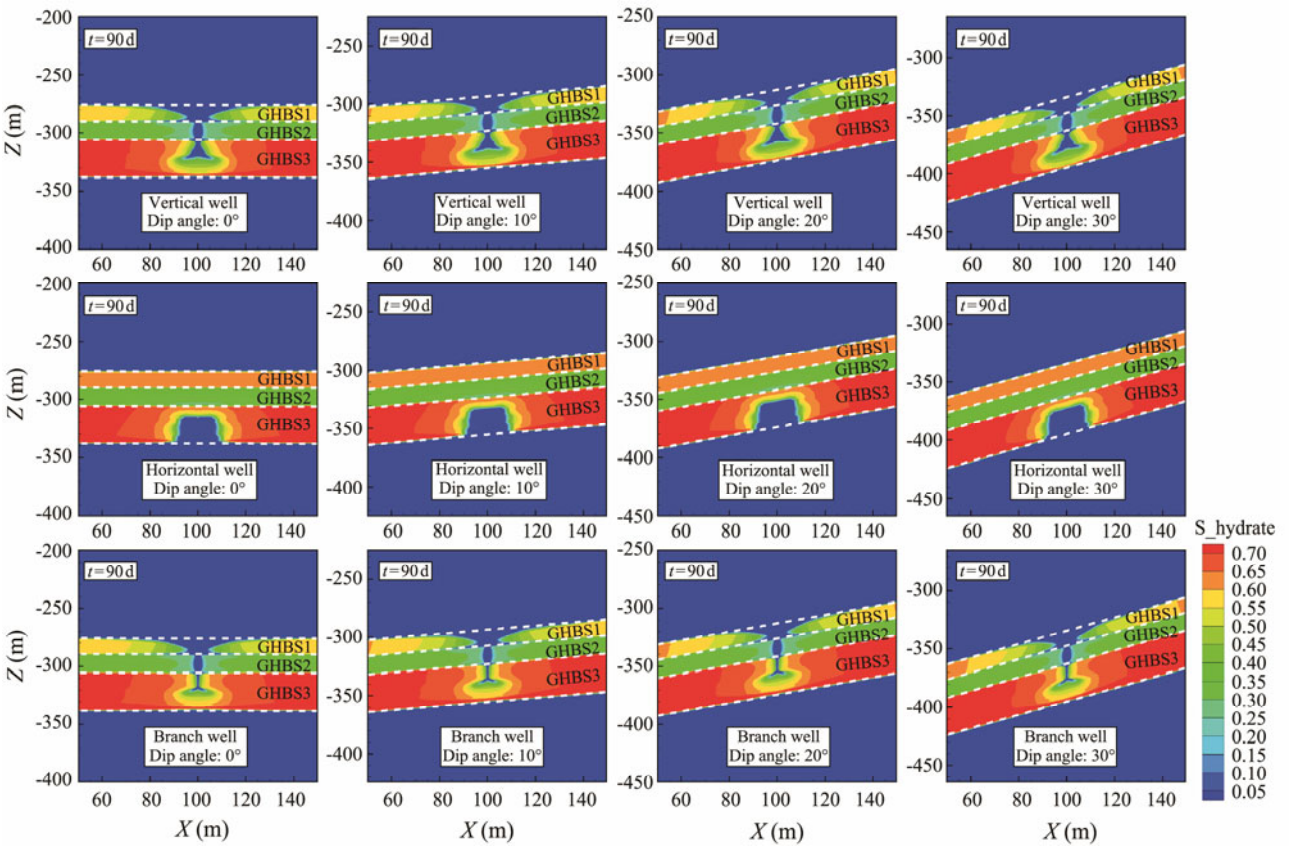

Fig.8 Spatial distribution of gas hydrate saturation in reservoirs with different dip angles at site AT1 (t=90 d, y=0 m).

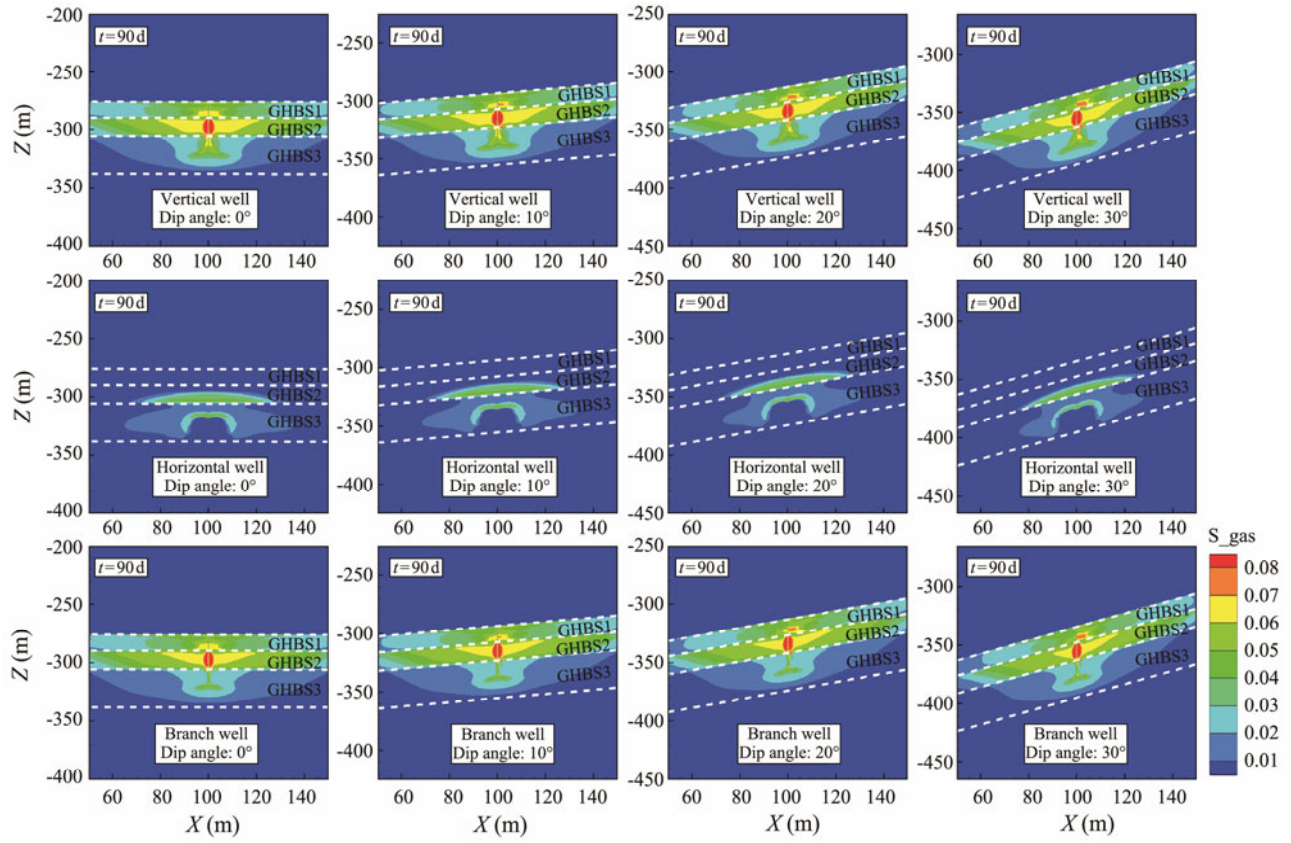

Fig.9 Spatial distribution of gas saturation in reservoirs with different dip angles at site AT1 (t=90 d, y=0 m).

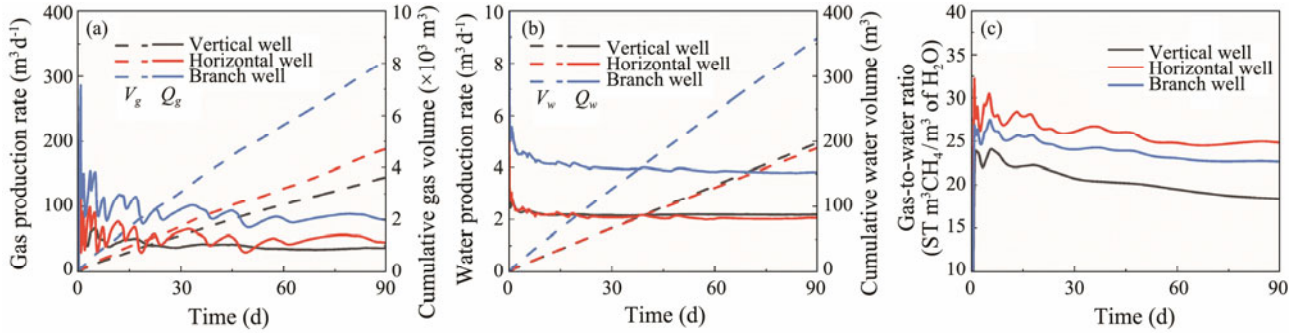

Fig.10 Gas and water production of short-term depressurization test at site W11 in the South China Sea.

terval of the multilateral wells is the longest, which effectively promotes the pressure drop transmission and hydrate dissociation in the reservoir (Fig.11). However, the production interval of the vertical well is connected with the overburden, allowing the free water in the permeable overburden to flow directly into the wellbore, thereby inhibiting depressurization (Fig.11). Fig.10b shows the evolution of water production in the inclined formations. The Q_w of the vertical well and horizontal well are similar, and the Q_w of the multilateral wells is highest due to the longest completion length, but all of them are lower than 10 $m^3\,d^{-1}$. By contrast, the horizontal well has the lowest V_w of 189.91 m^3 due to the water-blocking effect caused by the occurrence of hydrate (Fig.11), while the multilateral well has the highest water production of 359.25 m^3. The V_w of the vertical well is moderate and close to that of the horizontal well, which is about 197.70 m^3. Meanwhile, Fig.10c shows the corresponding evolutions of the R_{gw} under different conditions. Obviously, the R_{gw} of the horizontal well is the largest, followed by that of the multilateral wells, and the R_{gw} under the vertical well production is the lowest. This is also due to the lowest water production caused by the water-blocking effect when the horizontal well is adopted. For the multilateral wells, although the Q_g increases, the corresponding Q_w enhances more significantly, thereby giving rise to a lower R_{gw}.

3.2.2 Influence of formation dip

Fig.12 shows the percentage increments of the cumulative gas production and water recovery for three types of wells from reservoirs with different formation dip angles compared to the production results of horizontal reservoir. The increment of V_g using different types of wells is basically the same with the increase of formation dip, and

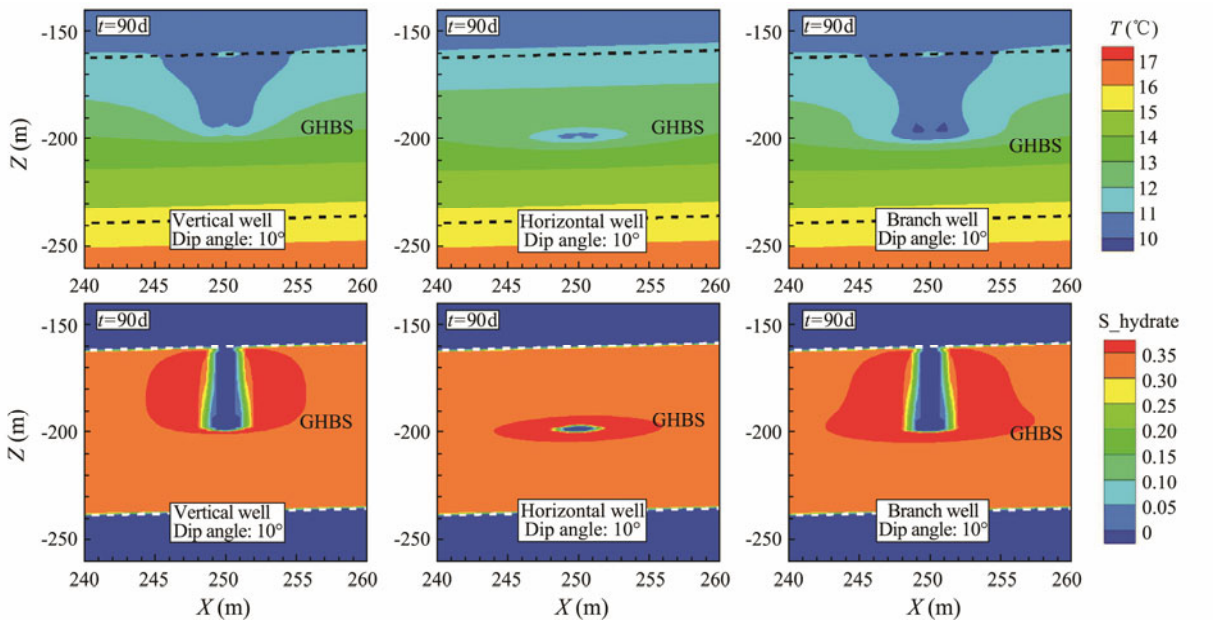

Fig.11 Spatial distributions of temperature and hydrate saturation at site W11 in the South China Sea (t=90 d, y=0 m).

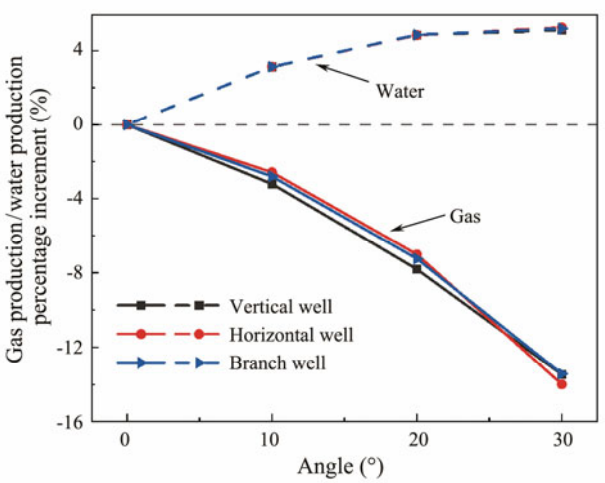

Fig.12 Percent increments of gas and water production of inclined reservoir at site W11 compared with horizontal formation in the South China Sea.

the larger the formation dip, the more significant the decline. When the formation dip increases to 30 degrees, the V_g decreases by about 14%. The corresponding increment of the V_w is almost the same. With the increase of formation dip, the increment of water production gradually slows down. When the formation dip is 30 degrees, the water production is about 6% higher than that of the horizontal formation. It is speculated that the reason for the above phenomena is also that the gas is more likely to escape at the upper dissociation front after the formation dip angle increases, while the fluid extraction at the lower hydrate dissociation front needs to overcome gravity (Figs.13 and 14). Moreover, the larger the formation dip is, the more obvious this difference may be. In addition, the influence of the formation dip on the short-term gas and water production in the low-permeability reservoir is almost the same across the three well types.

To sum up, in the low-permeability inclined hydrate reservoir, the gas and water production during depressurization are highly sensitive to the changes in formation dip, but not to the variations in well type. Therefore, the boreholes should also be deployed in the horizontal formation as far as possible.

4 Discussion

This section will focus on the short-term gas production performance of two typical inclined hydrate formations, and discuss the possible impact of reservoir permeability. Since the completion lengths of different types of wells in the two hydrate formations are different, the gas production per unit length (V_{gp}) is used to perform a comparative analysis (Wu *et al.*, 2021). Table 3 shows the gas production statistics of two sites under the condition of unit well length over 90 days. It is obvious that the reservoir permeability has a great influence on the V_{gp}, and the V_{gp} from the high-permeability reservoir is far greater than that from the low-permeability one. As shown in Table 3, the V_{gp} of the vertical well is the highest, the V_{gp} of the horizontal well is in the middle, and that of the multilateral wells is the lowest during the short-term depressurization in the high-permeability deposits. However, in the low-permeability sediments, the horizontal well produces the largest V_{gp}, followed by the multilateral wells, and the corresponding V_{gp} of the vertical well is the minimum. The possible reason for the differences is that the pressure drop propagation in the high-permeability reservoir is relatively faster, thus resulting in the strong inter-well interference in the production scene of multilateral wells, which leads to the minimum V_{gp}. Nevertheless, when the horizontal well is adopted, the invasion of water from the underlying formation will cause the decrease in gas production. In addition, the V_{gp} of the multilateral wells is lower than those of the vertical well and horizontal well, which also shows the significant

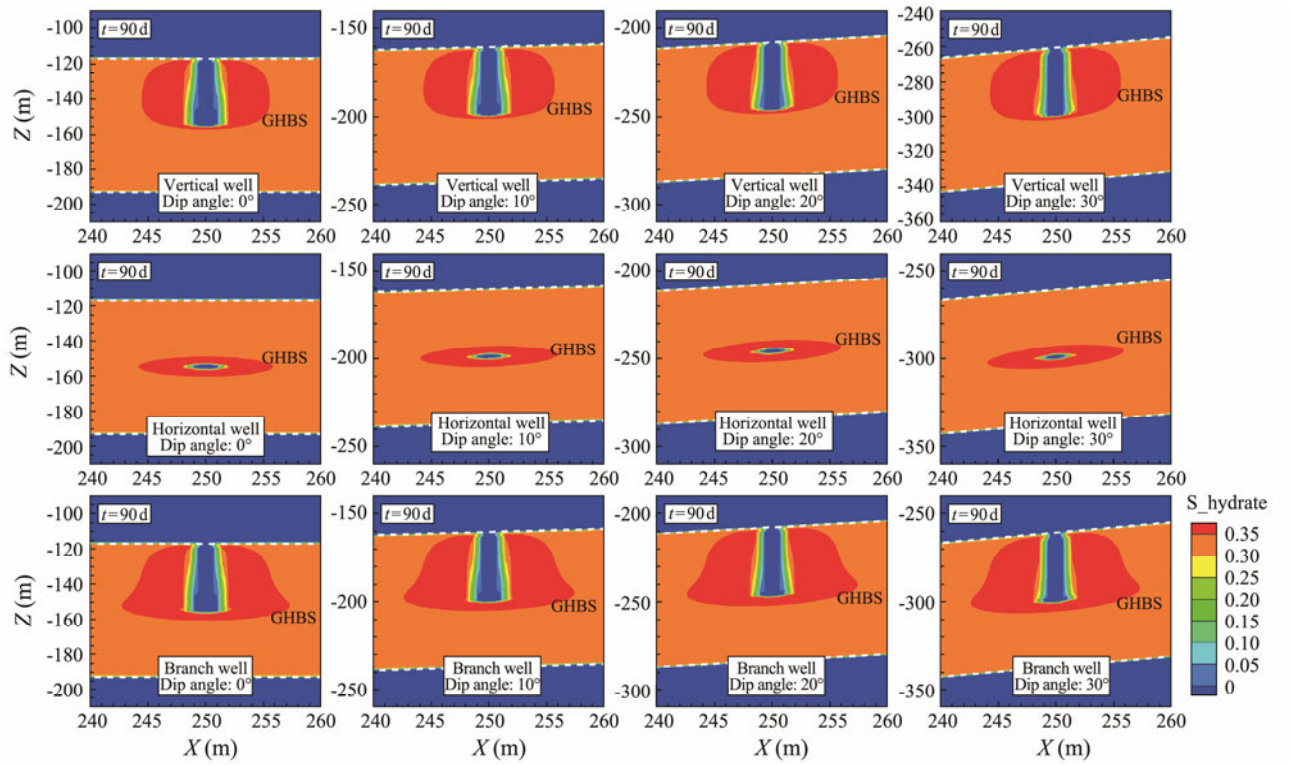

Fig.13 Spatial distribution of hydrate saturation in reservoirs with different dip angles at site W11 in South China Sea (t=90 d, y=0 m).

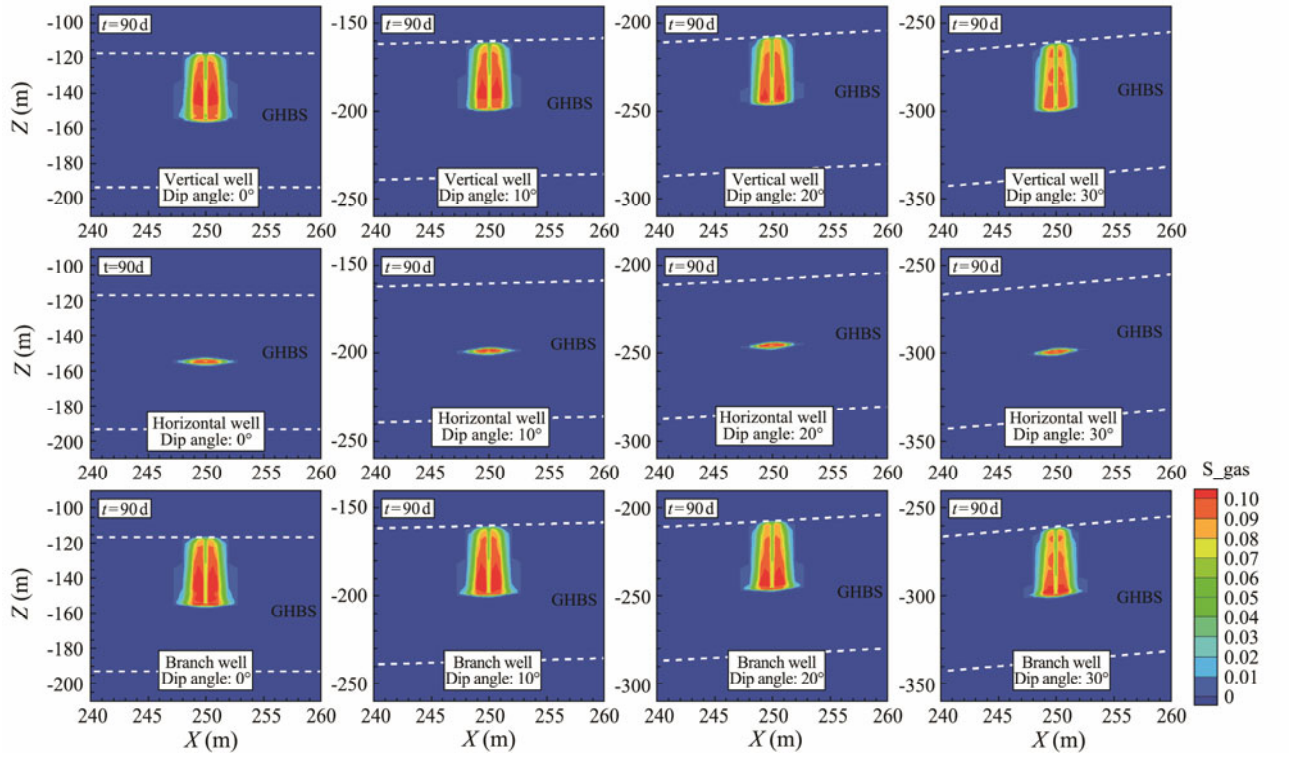

Fig.14 Spatial distribution of gas saturation in reservoirs with different dip angles at site W11 in the South China Sea (t=90 d, y=0 m).

inter-well interference. For the low-permeability reservoir, when employing the multilateral wells and vertical well, the depressurization effect will be weaker compared to using the horizontal well deployed in the middle of the reservoir because the production interval is directly connected with the permeable overburden. Besides, the low formation permeability hinders the rapid convective heat transfer between the overburden/underburden and the re-

servoir, which cannot quickly compensate the heat required for hydrate dissociation around the well. Meanwhile, due to the slow propagation of pressure drop in this formation, the inter-well interference may be negligible during the short-term production of the multilateral wells, and the synergistic effect is likely to dominate the production trial. Therefore, the horizontal well has the highest V_{gp}, and the V_{gp} of the multilateral wells is better than that of the vertical well.

Moreover, Fig.15 further compares the increment of V_{gp} and the evolution of R_{gw} for the two inclined reservoirs with those of the horizontal formation involving various types of production wells. Similarly, when the formation has a dip angle, the short-term V_{gp} will reduce, and the reduction will increase with the increase of the dip angle (Fig.15a). However, the variation of formation dip has a greater impact on the gas production for low-permeability reservoirs than high permeability ones. Within the range of 30 degrees for dip angles, the V_{gp} at site AT1 decreases by less than 6%. By contrast, at site W11, the V_{gp} has already exceeded a 6% decrease when the formation dip reaches 20 degrees, and the final V_{gp} will decrease by 14% if the dip angle further increases to 30 degrees. Obviously, the R_{gw} values corresponding to the two reservoirs with different permeabilities also show similar evolution trends. Specially, the R_{gw} in the high-permeability formation decreases slowly with the increase of formation dip, while that in the low-permeability formation decreases significantly (Fig. 15b). Besides, the R_{gw} in the low-permeability reservoir is higher than that in the high-permeability sediments. The possible reasons for the large difference in R_{gw} between two sites are the variations in permeability and irreducible water saturation. First, the permeability at site AT1 in the Nankai Trough in Japan is $k_x=k_y=1100$ mD, $k_z=500$ mD, and the permeability of site W11 in the South China Sea is $k_x=k_y=k_z=0.22$ mD. The quite different permeabilities at the two sites make their gas and water migration obviously different. In high-permeability reservoirs, the pressure drop transfer is relatively faster, thereby increasing the dissociation rate of hydrates. Therefore, a large amount of initial formation water and dissociated water will be extracted, which is likely to result in a relatively lower R_{gw}. However, the gas and water migration in low-permeability reservoirs is relatively slow, which may significantly decrease the water extraction and subsequently increase the R_{gw}. Second, the irreducible water saturations (S_{irA}) in sandy and silty reservoirs vary considerably. The high S_{irA} in the silty reservoir will give rise to a decrease in water recovery. Thus, the R_{gw} of the two sites is quite different. In addition, the differences in R_{gw} among different well types are also diverse. Obviously, the vertical well will have the inflow of free water from the overburden, resulting in the reduction in R_{gw}. The branch well is prone to impact of the inter-well interference between the vertical and the horizontal sections, which can reduce water extraction and give a relatively higher R_{gw}. As for the horizontal well, the water-blocking sections above and below the well prevent the water inflow from burdens, thereby resulting in a relatively higher R_{gw}. However, when the lower water-blocking section in the high-permeability reservoir is penetrated, a large amount of water from the underburden invades the wellbore, which leads to a rapid decrease in R_{gw}. By con-

Table 3 Statistical results of gas production per unit well length at two sites

Dip angle (°)	Site AT1			Site W11		
	Vertical well (m^3)	Horizontal well (m^3)	Multilateral wells (m^3)	Vertical well (m^3)	Horizontal well (m^3)	Multilateral wells (m^3)
0	45378.81	41945.95	25430.36	98.95	127.44	110.04
10	44973.33	41890.00	25201.90	95.79	124.15	106.96
20	44073.57	41329.76	24722.98	91.22	118.49	102.07
30	42645.71	40203.81	23981.67	85.63	109.61	95.27

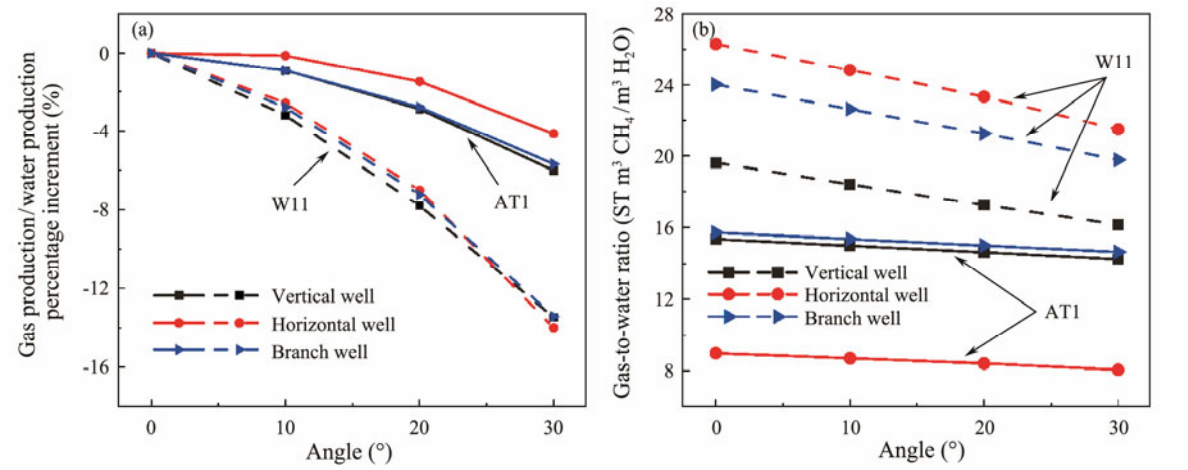

Fig.15 Increment of V_{gp} and evolution of R_{gw} at two sites with an increase in formation dip.

trast, this phenomenon does not appear in the low-permeability reservoir.

5 Conclusions and Suggestions

In this investigation, the short-term production performance of two typical marine hydrate reservoirs is studied, and the effects of formation dip and well type are systematically analyzed. The main conclusions and suggestions are as follows:

1) In the high-permeability hydrate reservoir at site AT1 of Japan, the scheme of multilateral wells can obtain the maximum gas production, and its gas-to-water ratio is basically the same as that of a vertical well. A higher gas-to-water ratio is available when a single horizontal well is used for production trial, but the gas production rate will be greatly reduced due to the water invasion from the underburden after the full hydrate dissociation below the well, thereby resulting in a significant decline in the gas-to-water ratio.

2) For the low-permeability hydrate reservoir in the South China Sea, the gas production rates are essentially low across three types of wells. The gas production rate of the multilateral wells is the highest, followed by that of the horizontal well, and the production rate of the vertical well is the lowest. However, the corresponding gas-to-water ratio is the highest in the horizontal well, followed by that of the multilateral wells, with the lowest ratio observed in the vertical well.

3) The influence of formation dip angles on the production performance for different well types is basically the same, whether in the high or low permeability formation. The inclined formation will reduce the gas production rate when the hydrate dissociation is triggered by depressurization, and simultaneously increase the water extraction rate. The larger the dip angle is, the more pronounced the decrease of gas production rate. Therefore, the boreholes should be deployed in the horizontal formation as far as possible during hydrate exploitation.

4) For different types of production wells, the gas production per unit well length is higher when the vertical well is adopted in high-permeability reservoirs during production trials. Conversely, horizontal wells can obtain greater gas production per unit well length in low-permeability sediments. In addition, the formation dip has a negligible effect on the gas production per unit length for different well types, but when the formation dip is the same, the gas production of the low-permeability reservoir decreases more obviously.

Nomenclatures

Q_g, gas production rate (ST $m^3 d^{-1}$)
Q_w, water production rate (ST $m^3 d^{-1}$)
V_g, total gas production (ST m^3)
V_{gp}, gas production per unit well length (ST m^3)
R_{gw}, gas-to-water ratio (ST m^3 CH_4/ST m^3 H_2O)
P_{pw}, hydrostatic pore water pressure (MPa)
P_{atm}, standard atmospheric pressure (MPa)
h, water depth (m)
z, depth of sediment from the seafloor (m)
g, acceleration due to gravity ($m s^{-2}$)
ρ_{sw}, average sea water density ($kg m^{-3}$)
T, temperature (℃)
T_0, geothermal gradient (℃)
ΔT, geothermal gradient (℃ m^{-1})

Acknowledgements

This work was supported by the National Natural Science Foundation of China (Nos. 42372361 and 51904280), and the Key Research and Development Program of China (No. 2018YFE0126400).

References

Boswell, R. J., 2013. Japan completes first offshore methane hydrate production test-methane successfully produced from deep-water hydrate layers. *Center for Natural Gas Oil*, **412** (1): 386-7614.

Bu, Q., Hu, G., Liu, C., Dong, J., Xing, T., Sun, J., *et al*., 2021. Effect of methane gas on acoustic characteristics of hydrate-bearing sediment-model analysis and experimental verification. *Journal of Ocean University of China*, **20** (1): 75-86, https://doi.org/10.1007/s11802-021-4354-7.

Cao, X., Sun, J., Ning, F., Zhang, H., Wu, N., and Yu, Y., 2022. Numerical analysis on gas production from heterogeneous hydrate system in Shenhu area by depressurizing: Effects of hydrate-free interlayers. *Journal of Natural Gas Science and Engineering*, **101**: 104504, https://doi.org/10.1016/j.jngse.2022.104504.

Chen, L., Feng, Y., Merey, S., Lijith, K. P., Singh, D. N., Komiya, A., *et al*., 2020a. Numerical investigation on gas production from Shenhu (China): Influence of layer inclination and horizontal inhomogeneities. *Journal of Natural Gas Science and Engineering*, **82**: 103509.

Chen, Q., Hu, G. W., Wu, N. Y., Liu, C. L., Meng, Q. G., Li, C. F., *et al*., 2020b. Evaluation of clayed silt properties on the behavior of hydrate production in South China Sea. *China Geology*, **3** (3): 362-368, https://doi.org/10.31035/cg2020050.

Dong, L., Li, Y., Liu, C., Liao, H., Chen, G., Chen, Q., *et al*., 2019. Mechanical properties of methane hydrate-bearing interlayered sediments. *Journal of Ocean University of China*, **18** (6): 1344-1350, https://doi.org/10.1007/s11802-019-3929-z.

Dou, X. F., Ning, F. L., Li, Y. L., Liu, C. L., Sun, J. X., Li, Y., *et al*., 2020. Continuum-discrete coupling method for numerical simulation of sand production from hydrate reservoirs: A lab-scale case study. *Acta Petrolei Sinica*, **41** (5): 629-642 (in Chinese with English abstract).

Fujii, T., Noguchi, S., Takayama, T., Suzuki, K., Yamamoto, K., and Saeki, T., 2013. Site selection and formation evaluation at the 1st offshore methane hydrate production test site in the eastern Nankai Trough, Japan. *75th EAGE Conference & Exhibition – Workshop*s. European Association of Geoscientists & Engineers, cp-349.

Gu, Y., Sun, J., Qin, F., Ning, F., Cao, X., Liu, T., *et al*., 2023. Enhancing gas recovery from natural gas hydrate reservoirs in the eastern Nankai Trough: Deep depressurization and underburden sealing. *Energy*, **262**: 125510.

Gu, Y., Sun, J., Qin, F., Ning, F., Li, Y., Cao, X., *et al*., 2022. Numerical analysis on gas production from silty hydrate reservoirs in the South China Sea by depressurizing: The effect of permeability reduction caused by pore compression. *Journal of Natural Gas Science and Engineering*, **104**: 104680,

https://doi.org/10.1016/j.jngse.2022.104680.

Hancock, S., Collett, T., Dallimore, S., Satoh, T., Inoue, T., Huenges, E., *et al*., 2005. Overview of thermal-stimulation production-test results for the JAPEX/JNOC/GSC *et al*. Mallik 5l-38 gas hydrate production research well. *Scientific Results from the Mallik 2002 Gas Hydrate Production Research Well Program, Mackenzie Delta, Northwest Territories, Canada*. Geological Survey of Canada, CD-ROM.

Huang, L., Kang, J. L., Shen, X. D., Sun, J. Y., Meng, Q. G., Chen, Q., *et al*., 2022. Experimental investigation of hydrate formation in water-dominated pipeline and its influential factors. *China Geology*, **5**: 1-12, https://doi.org/10.31035/cg2022015.

Ji, Y. K., Liu, C. L., Zhang, Z., Meng, Q. G., Liu, L. L., Zhang, Y. C., *et al*., 2022. Experimental study on characteristics of pore water conversion during methane hydrate formation in unsaturated sand. *China Geology*, **5** (2): 1-9, https://doi.org/10.31035/cg2022013.

Kurihara, M., Sato, A., Ouchi, H., Narita, H., Ebinuma, T., Suzuki, K., *et al*., 2010. Gas hydrate: Prediction of production test performances in eastern Nankai Trough methane hydrate reservoirs using 3D reservoir model. *Offshore Technology Conference*. Houston, OTC-20737-MS.

Li, J. F., Ye, J. L., Qin, X. W., Qiu, H. J., Wu, N. Y., Lu, H. L., *et al*., 2018a. The first offshore natural gas hydrate production test in South China Sea. *China Geology*, **1** (1): 5-16, https://doi.org/10.31035/cg2018003.

Li, Q., Cheng, Y., Zhang, H., Yan, C., and Liu, Y., 2018b. Simulating the effect of hydrate dissociation on wellhead stability during oil and gas development in deepwater. *Journal of Ocean University of China*, **17** (1): 35-45, https://doi.org/10.1007/s11802-018-3544-4.

Li, X. S., Xu, C. G., Zhang, Y., Ruan, X. K., Li, G., and Wang, Y., 2016. Investigation into gas production from natural gas hydrate: A review. *Applied Energy*, **172**: 286-322, https://doi.org/10.1016/j.apenergy.2016.03.101.

Li, Y. L., Wan, Y. Z., Chen, Q., Sun, J. X., Wu, N. Y., Hu, G. W., *et al*., 2019a. Large borehole with multi-lateral branches: A novel solution for exploitation of clayey silt hydrate. *China Geology*, **2** (3): 331-339, https://doi.org/10.31035/cg2018082.

Li, Y. L., Wu, N. Y., Ning, F. L., Hu, G. W., Liu, C. L., Dong, C. Y., *et al*., 2019b. A sand-production control system for gas production from clayey silt hydrate reservoirs. *China Geology*, **2** (2): 121-132, https://doi.org/10.31035/cg2018081.

Mao, P., Sun, J., Ning, F., Chen, L., Wan, Y., Hu, G., *et al*., 2021a. Numerical simulation on gas production from inclined layered methane hydrate reservoirs in the Nankai Trough: A case study. *Energy Reports*, **7**: 8608-8623, https://doi.org/10.1016/j.egyr.2021.03.032.

Mao, P., Wan, Y., Sun, J., Li, Y., Hu, G., Ning, F., *et al*., 2021b. Numerical study of gas production from fine-grained hydrate reservoirs using a multilateral horizontal well system. *Applied Energy*, **301**: 117450, https://doi.org/10.1016/j.apenergy.2021.117450.

Mi, F., He, Z., Fang, B., Ning, F., and Jiang, G., 2022a. Molecular insights into the effects of surface property and pore size of non-swelling clay on methane hydrate formation. *Fuel*, **311**: 122607.

Mi, F., He, Z., Jiang, G., and Ning, F., 2022b. Effects of marine environments on methane hydrate formation in clay nanopores: A molecular dynamics study. *The Science of the Total Environment*, **852**: 158454.

Mi, F., He, Z., Zhao, Y., Jiang, G., and Ning, F., 2022c. Effects of surface property of mixed clays on methane hydrate formation in nanopores: A molecular dynamics study. *Journal of Colloid and Interface Science*, **627**: 681-691.

Moridis, G. J., 2008. TOUGH+Hydrate v1.0 user's manual: A code for the simulation of system behavior in hydrate-bearing geologic media. Online: https://digital.library.unt.edu/ark:/67531/metadc896271.

Ning, F., Chen, Q., Sun, J., Wu, X., Cui, G., Mao, P., *et al*., 2022. Enhanced gas production of silty clay hydrate reservoirs using multilateral wells and reservoir reformation techniques: Numerical simulations. *Energy*, **254**: 124220, https://doi.org/10.1016/j.energy.2022.124220.

Ning, F. L., Liang, J. Q., Wu, N. Y., Zhu, Y. H., Wu, S. G., Liu, C. L., *et al*., 2020. Reservoir characteristics of natural gas hydrates in China. *Natural Gas Industry*, **40** (8): 1-24 (in Chinese with English abstract).

Schoderbek, D., Farrell, H., Howard, J., Raterman, K., Silpngarmlert, S., Martin, K., *et al*., 2013. Conocophillips gas hydrate production test. Conocophillips Co., Houston. https://doi.org/10.2172/1123878.

Sloan, E. D. J., 2003. Fundamental principles and applications of natural gas hydrates. *Nature*, **426** (6964): 353-359.

Song, B., Cheng, Y., Yan, C., Lyu, Y., Wei, J., Ding, J., *et al*., 2019. Seafloor subsidence response and submarine slope stability evaluation in response to hydrate dissociation. *Journal of Natural Gas Science and Engineering*, **65**: 197-211, https://doi.org/10.1016/j.jngse.2019.02.009.

Song, Y., Yang, L., Zhao, J., Liu, W., Yang, M., Li, Y., *et al*., 2014. The status of natural gas hydrate research in China: A review. *Renewable and Sustainable Energy Reviews*, **31**: 778-791.

Sun, J., Gu, Y., Qin, F., Ning, F., Li, Y., Cao, X., *et al*., 2022. Key factors analyses for prediction of accurate gas production rate in hydrate reservoirs during model construction. *Journal of Natural Gas Science and Engineering*, **102**: 104566, https://doi.org/10.1016/j.jngse.2022.104566.

Sun, J., Ning, F., Lei, H., Gai, X., Sánchez, M., Lu, J., *et al*., 2018. Wellbore stability analysis during drilling through marine gas hydrate-bearing sediments in Shenhu area: A case study. *Journal of Petroleum Science and Engineering*, **170**: 345-367.

Sun, J., Ning, F., Liu, T., Li, Y., Lei, H., Zhang, L., *et al*., 2021a. Numerical analysis of horizontal wellbore state during drilling at the first offshore hydrate production test site in Shenhu area of the South China Sea. *Ocean Engineering*, **238**: 109614.

Sun, J., Ning, F., Liu, T., Liu, C., Chen, Q., Li, Y., *et al*., 2019. Gas production from a silty hydrate reservoir in the South China Sea using hydraulic fracturing: A numerical simulation. *Energy Science & Engineering*, **7** (4): 1106-1122, https://doi.org/10.1002/ese3.353.

Sun, J., Ning, F., Zhang, L., Liu, T., Peng, L., Liu, Z., *et al*., 2016. Numerical simulation on gas production from hydrate reservoir at the 1st offshore test site in the eastern Nankai Trough. *Journal of Natural Gas Science and Engineering*, **30**: 64-76, https://doi.org/10.1016/j.jngse.2016.01.036.

Sun, J. X., Ning, F. L., Zheng, M. M., Zhang, L., Liu, T. L., Jiang, G. S., *et al*., 2015. Numerical simulation on natural gas hydrate formation within porous media using constant volume method. *Natural Gas Geoscience*, **26** (11): 2172-2184 (in Chinese with English abstract).

Sun, J. X., Zhang, L., Ning, F. L., Lei, H. W., Liu, T. L., Hu, G. W., *et al*., 2017. Production potential and stability of hy-drate-bearing sediments at the site GMGS3-W19 in the South China Sea: A preliminary feasibility study. *Marine and Petroleum Geology*, **86**: 447-473.

Sun, J. X., Zhang, L., Ning, F. L., Liu, T. L., Fang, B., Li, Y. L., *et al*., 2021b. Research status and prospects of increasing production from gas hydrate reservoirs. *Acta Petrolei Sinica*, **42**

(4): 523-540 (in Chinese with English abstract).

Sun, J. X., Zhao, H. B., Cao, X. X., and Mao, P. X., 2021c. Numerical simulation on depressurization-induced gas production from hydrate reservoirs in the Liwan area, South China Sea using horizontal well. *Science Technology and Engineering*, **21** (24): 10246-10256 (in Chinese with English abstract).

Wang, P., Zhu, Y., Lu, Z., Bai, M., Huang, X., Pang, S., *et al*., 2018. Research progress of gas hydrates in the Qilian Mountain permafrost, Qinghai, Northwest China: Review. *Scientia Sinica Physica, Mechanica & Astronomica*, **49** (3): 034606, https://doi.org/10.1360/sspma2018-00133.

Wu, N. Y., Liu, C. L., and Hao, X. L., 2018. Experimental simulations and methods for natural gas hydrate analysis in China. *China Geology*, **1** (1): 61-71, https://doi.org/10.31035/cg2018008.

Wu, N., Li, Y., Wan, Y., Sun, J., Huang, L., and Mao, P., 2021. Prospect of marine natural gas hydrate stimulation theory and technology system. *Natural Gas Industry*, **8** (2): 100-115 (in Chinese with English abstract).

Xu, M., Fang, X., Ning, F., Ou, W., Zhang, L., and Wang, D., 2021. Effect of hydrophilic silica nanoparticles on hydrate formation during methane gas migration in a simulated wellbore. *Petroleum*, **7** (4): 485-495, https://doi.org/10.1016/j.petlm.2021.11.004.

Yamamoto, K., and Dallimore, S. J. N. G., 2008. Aurora-JOGMEC-NRCan Mallik 2006–2008 gas hydrate research project progress. *Fire in the Ice–Mathane Hydrate Newsletter*. The National Energy Technology Laboratory, 1-5.

Yamamoto, K., Wang, X. X., Tamaki, M., and Suzuki, K., 2019. The second offshore production of methane hydrate in the Nankai Trough and gas production behavior from a heterogeneous methane hydrate reservoir. *RSC Advances*, **9** (45): 25987-26013, https://doi.org/10.1039/c9ra00755e.

Yuan, Y., Xu, T., Xia, Y., and Xin, X., 2018. Effects of formation dip on gas production from unconfined marine hydrate-bearing sediments through depressurization. *Geofluids*, **2018**: 1-11.

Zhang, W., Liang, J., Wei, J., Lu, J. A., Su, P., Lin, L., *et al*., 2020. Geological and geophysical features of and controls on occurrence and accumulation of gas hydrates in the first offshore gas-hydrate production test region in the Shenhu area, northern South China Sea. *Marine and Petroleum Geology*, **114**: 104191, https://doi.org/10.1016/j.marpetgeo.2019.104191.

Zhang, Z. C., Wu, N. Y., Liu, C. L., Hao, X. L., Zhang, Y. C., Gao, K., *et al*., 2022. Molecular simulation studies on natural gas hydrate nucleation and growth: A review. *China Geology*, **5** (2): 1-15, https://doi.org/10.31035/cg2022017.

(Edited by Chen Wenwen)